


 Cite this: *RSC Adv.*, 2023, **13**, 11733

# Intrafibrillar mineralization of type I collagen by micelle-loaded amorphous calcium phosphate nanoparticles†

 Hongyu Xie,†<sup>a</sup> Jian Sun,‡<sup>b</sup> Fangfang Xie\*<sup>a</sup> and Shengbin He \*<sup>b</sup>

Mineralization of type I collagen fibrils is highly desired for artificial bone preparation and teeth repairing. Generally, amorphous calcium phosphate (ACP) combined with non-collagenous protein analogue (NCPA) were used for biomimetic remineralization of collagen fibrils. However, the ACP was likely to aggregate to form larger particles that could not infiltrate into the gaps of the collagen for intrafibrillar mineralization, and the poor storage stability of ACP has challenged its practical applications. To address this question, here we assembled ACP that was stabilized by carboxylated polyamidoamine (CPAMAM) at a pH of 6.5 to form dispersed nanoparticles of 25 nm in size, which was named as ACP/CPAMAM. The ACP/CPAMAM nanoparticles were further loaded into micelles composed of polysorbate and polyethylene glycol (PEG) to further improve their storage stability. The micelle-loaded ACP/CPAMAM particles could maintain their amorphous phase after storage for 12 months. During the mineralization of collagen fibrils, isopropanol (IPA) was introduced to dissolve the micelles and release the ACP/CPAMAM nanoparticles. By using micelle-loaded ACP/CPAMAM, good intrafibrillar mineralization of type I collagen was demonstrated. This work provides novel methods for preparing ACP nanoparticles with good storage stability and controllable release for intrafibrillar mineralization.

Received 27th February 2023

Accepted 10th April 2023

DOI: 10.1039/d3ra01321a

[rsc.li/rsc-advances](https://rsc.li/rsc-advances)

## 1. Introduction

Biomaterials such as teeth and bones are composites of an inorganic component, predominantly hydroxyapatite (HAP), and an organic component, predominantly type I collagen. The HAP nanocrystalline fits within the gap zones of type I collagen molecules, endowing the biomaterials with reasonable hardness and toughness to perform their skeleton functions. Demineralization happened frequently in dental caries, dental erosion, and bone lesions.<sup>1–4</sup> Once the biomaterials begin to be demineralized pathologically or intentionally, collagen fibrils become exposed to endogenous protease and are degraded. As a result, the biomaterial structure would be disintegrated, and its hardness and toughness were decreased. To solve this problem, remineralization of collagen has been widely investigated as thoroughly methods for teeth repairing and bone reconstruction.<sup>5–8</sup>

The most widely used methods for remineralization of collagen were to develop calcium phosphate (CaP) microparticles of 1–5 μm in size or amorphous calcium phosphate (ACP) nanoparticles of 30–500 nm in size.<sup>9–11</sup> Both of them could release Ca and P ions to the peripheral matrix of collagen for the subsequent mineralization. The ACP nanoparticles had higher surface area to volume ratio and released higher levels of Ca and P ions than CaP microparticles, and hence became very popular in recent years. Because ACP would transform easily into a thermodynamically more stable HAP crystalloid, biomimetic analogs of non-collagenous proteins were generally used to transiently stabilize the ACP and guide the nucleation during crystallization process.<sup>12–15</sup> However, the ACP was likely to aggregate to form larger particles that could not infiltrate directly into the gaps of the collagen (40 nm) for intrafibrillar mineralization, and the released Ca and P ions deposited outside the fibrillar collagen to form HAP for extrafibrillar mineralization.<sup>16,17</sup> Additionally, the poor storage stability of ACP has challenged its practical applications.

Intrafibrillar mineralization of collagen not only increases the mechanical stability of the biomaterial, but also protects the collagen molecules from external challenges, such as bacterial degradation and endogenous enzymolysis.<sup>18–21</sup> In the present work, we assembled ACP of about 25 nm in size, which were stabilized by carboxylated polyamidoamine (CPAMAM) to form dispersed ACP/CPAMAM nanoparticles, as shown in Fig. 1. The ACP/CPAMAM nanoparticles were further loaded into micelles composed of polysorbate and polyethylene glycol (PEG) to

<sup>a</sup>College of Stomatology, Hospital of Stomatology, Guangxi Medical University, Nanning, Guangxi 530021, P. R. China. E-mail: xiedualfang@163.com

<sup>b</sup>Key Laboratory of Longevity and Aging-related Diseases of Chinese Ministry of Education, Guangxi Colleges and Universities Key Laboratory of Biological Molecular Medicine Research, School of Basic Medical Sciences, Guangxi Medical University, Nanning, Guangxi 530021, P. R. China. E-mail: comhsb@163.com

† Electronic supplementary information (ESI) available. See DOI: <https://doi.org/10.1039/d3ra01321a>

‡ These authors contributed equally to this work.



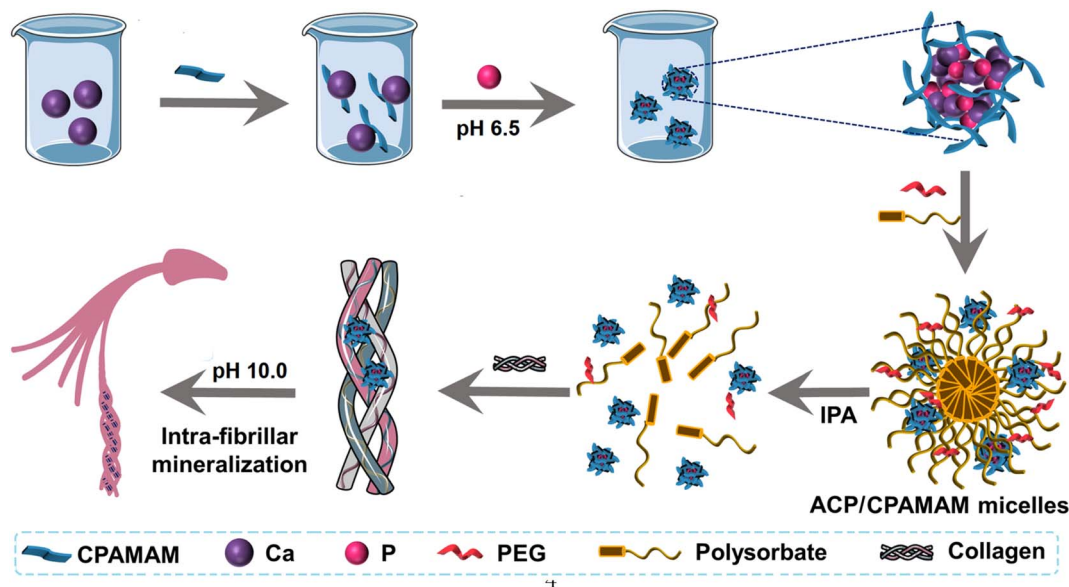


Fig. 1 Schematic diagrams for assembling micelle-loaded ACP/CPAMAM nanoparticles.

further improve their storage stability. During the mineralization of collagen fibrils, isopropyl alcohol (IPA) was introduced to dissolve the micelles and release the ACP/CPAMAM nanoparticles. The small sizes of the ACP/CPAMAM nanoparticles enable them to infiltrate directly into the gaps of the collagen for intrafibrillar mineralization. By using the micelle-loaded ACP/CPAMAM nanoparticles, good intrafibrillar mineralization of type I collagen was demonstrated.

## 2. Materials and methods

### 2.1. Synthesis of ACP/CPAMAM nanoparticles

CPAMAM of 158 mg was added to 25 mL  $\text{CaCl}_2$  solution (10 mM). The mixture was incubated at room temperature for 24 h, and its pH was adjusted to 6.0 by NaOH/HCl. Then 25 mL  $\text{Na}_2\text{HPO}_4$  (6 mM) was added to the mixture. The mixture was stirred for various reaction times (1 min, 30 min, 60 min, 120 min) at room temperature. The final mineralization solution exhibited a pH of 6.5 without any precipitate. The mixed solutions were then subjected to ultracentrifugation (Beckman Coulter, Fullerton, CA, USA) at 100 000 g for 1 h at 4 °C, and the supernatant was removed.

The surface characteristics and corresponding histograms representing diameter size distribution of the ACP/CPAMAM nanoparticles were observed using TEM (Talos F200X, FEI, USA). Prior to the observations, the samples were prepared by placing a drop of ACP/CPAMAM solution on a 400 formvar-coated Ni transmission electron microscope grid and allowing it to air-dry at 25 °C. Meanwhile, the distribution of calcium and phosphorus inside the samples was determined *via* STEM-EDX mapping (Talos F200X, FEI, USA), and the crystallinity of the minerals was confirmed using SAED (Talos F200X, FEI, USA). DLS measurements were used to obtain zeta potentials (Nano ZS90, Malvern, the UK) of the samples. Additionally, the chemical bonds of the ACP/CPAMAM nanoparticles were

analyzed using Fourier transform infrared (FTIR) spectroscopy (Nicolet iS10, Thermo Fisher Scientific, USA).

### 2.2. Preparation of micelles-loaded ACP/CPAMAM nanoparticles

PEG-6000 (30 mg  $\text{mL}^{-1}$ , Shenggong Bioengineering Co., Ltd., China) was dissolved in the ACP/CPAMAM solution and reacted for 30 min. Polysorbate (ranging from 50, 100, 350, 500, and 1000 mg  $\text{mL}^{-1}$ ) was slowly added to the solution, and the mixture was stirred for 3 h at room temperature. The micelles were then obtained by centrifuging the micelles solution at 100 000 rcf for 1 h at 4 °C to remove the supernatant containing the free calcium and phosphate ions. After centrifugation, the supernatant was collected to determine the concentration of calcium ions using inductively coupled plasma-optical emission spectrometry (ICP-OES) (73, Agilent, USA) to calculate the encapsulation efficiency (EE) through the following formula:

$$EE = \frac{\text{total Ca}^{2+} - \text{free Ca}^{2+}}{\text{total Ca}^{2+}} \times 100\% \quad (1)$$

The morphology of micelle-loaded ACP/CPAMAM and micelle-loaded ACP was observed using TEM; the distribution of ACP/CPAMAM nanoparticles in the samples was determined *via* STEM-EDX mapping. The crystallinity of the minerals was validated using SAED. The hydrodynamic diameter and the zeta potentials of the samples were measured using a Zeta sizer Nano ZS detector. Additionally, the chemical bonds of the micelle-loaded ACP/CPAMAM and empty micelles were analyzed using a Raman DXR spectrometer (Thermo Scientific, Waltham, MA, USA).

### 2.3. Release of ACP/CPAMAM nanoparticles mediated *via* IPA

To destroy the structure of micelles and release the ACP/CPAMAM nanoparticles as the mineralization medium, we



added IPA of various concentrations (0.1, 0.2, 0.4, and 0.6 g mL<sup>-1</sup>) into the micelle-loaded ACP/CPAMAM at pH 6.5, the solutions were then subjected to vortex mixing for 10 min, followed by ultracentrifugation at 10 000 rcf for 60 min at 4 °C. The final concentrations of calcium ions in the solution were then measured *via* ICP-OES, and the state of the ACP/CPAMAM nanoparticles was observed *via* TEM. Additionally, DLS measurements were used to obtain zeta potentials of the samples.

#### 2.4. Preparation and intrafibrillar mineralization of type I collagen by micelle-loaded ACP/CPAMAM nanoparticles

Collagen fibrils were self-assembled by dissolving type I collagen in 0.02 M hydrochloric acid overnight at 4 °C, and 2 µg mL<sup>-1</sup> phenol red (Shenggong Bioengineering Co., Ltd., China) was added to the solution. Subsequently, 65 µL collagen solution was placed on a Petri dish, on which a 400-mesh, carbon-coated, formvar-coated Ni transmission electron microscope grid (Zhongjingkeyi, P. R. China) was placed. The collagen solution was then neutralized using 25% ammonium hydroxide solution (v/v), which was indicated by the color change from red to yellow of the pH indicator, and the neutralized collagen solution was left to gel *via* incubating at 37 °C for 24 h. The as-constructed collagen was then crosslinked using a 0.03 M 1-ethyl-3-(3-dimethylaminopropyl)-carbodiimide (EDC)/0.06 M *N*-hydroxysuccinimide (Yuanye, Bioengineering, Co., Ltd., China) solution for 4 h. For the subsequent tests, the grids were briefly cleaned three times using deionized water and air-dried. The structures and diameters of collagen fibrils were then observed and measured using TEM.

The collagen-coated grids were floated upside down over 200 µL of the ACP nanoparticles and ACP/CPAMAM nanoparticles mediated *via* IPA in a chamber with 100% humidity for 3 d, respectively, and the mineralization mediums was replaced every 24 h. Subsequently, the mineralization of collagen fibrils was observed using TEM at 80 kV for 72 h, after which the grids were washed three times with deionized water and then dried in air. The remineralization of collagen fibrils and the crystal properties of the formed minerals inside of the collagen fibrils were subsequently observed and analyzed using TEM and STEM-EDX mapping.

#### 2.5. Extrafibrillar mineralization of type I collagen fibrils tablet by micelle-loaded ACP/CPAMAM nanoparticles

Twenty-four sound human third molars were obtained and approved by the Ethics Committee of the Department of Oral and Maxillofacial Surgery of the Affiliated Stomatological Hospital of Guangxi Medical University with a scalpel blade removed the organic contaminants. Then the teeth were treated with 3% sodium hypochlorite to remove bacteria, which were stored in 0.5% thymol at 4 °C and used in a month. Using a low-speed water cooled diamond saw (Isomet, Buehler, Lake Bluff, IL, USA), the teeth were cut perpendicular to the long axis of tooth, above the cement–enamel junction (CEJ) to prepared into a 5 × 5 × 1 mm dentin specimen. After polishing and ultrasonic cleaning, the human dentin grinding tablets were

prepared, then the samples ( $n = 8$ ) were immersed in 0.5 M EDTA (pH 8.0) (Shenggong Bioengineering Co., Ltd., China) solution at 25 °C for 30 min to remove the smear layer, others were demineralized with 0.5 M EDTA (pH 8.0) (Shenggong Bioengineering Co., Ltd., China) solution at 25 °C for 7d, Further, the samples were immersed in guanidine chloride (GuCl, 4 M) (Shenggong Bioengineering Co., Ltd., China) to remove the non-collagen protein for 24 h. Finally, the specimens ( $n = 8$ ) were rinsed with 1 mL of ACP/CPAMAM nanoparticles mediated *via* IPA in a chamber with 100% humidity with the remineralizing solution was changed every day. After remineralization for 15 days, the dentin discs were washed three times with deionized water and ultrasonicated for 10 min. The qualitatively characterize the demineralization degree of these dentin discs were analyzed using scanning electron microscopy (SEM; SU8020, Hitachi, Japan) operating at 20 kV.

### 3. Results and discussion

#### 3.1. ACP/CPAMAM nanoparticles with good monodispersity were synthesized

Intrafibrillar mineralization cannot be achieved by simply immersing collagen fibrils in Ca/P solutions; it requires the use of nucleation inhibitors to stabilize the Ca/P relevant complexes and prevent them from crystallizing outside the fibrils. In biomineralization, non-collagenous protein analogues (NCPAs), such as osteopontin and dentin matrix proteins provide as nucleation inhibitors and/or templates to guide intrafibrillar mineralization orderly.<sup>2,22</sup> However, they are not economically viable for clinical research due to technical limitations in the extraction and preservation.<sup>23,24</sup> Carboxylated polyamidoamine (CPAMAM) is a highly-branched polymer characterized by the presence of multiple carboxyls to simulate the NCPA functions. Although the combination of ACP and CPAMAM has been used previously,<sup>10,25,26</sup> these studies mainly focused on preparing ACP/CPAMAM in alkaline condition (pH 9–10) to form large and aggregated ACP particles. The large and aggregated ACP particles are unfavorable for intrafibrillar mineralization, because they cannot infiltrate into the gaps of the collagen.

To obtain ACP nanoparticles with size smaller than the gap of the collagen, here three methods were used for preparing ACP: (1) without stabilizer; (2) with CPAMAM as a stabilizer in alkaline condition (pH = 10.0); (3) with CPAMAM as a stabilizer in weak acidic condition (pH = 6.5). As shown in Fig. 2a1–a4, after mixing Ca and P for 1 min, the Ca/P mixture transformed fleetly to crystal phase, which is similar with the results described previously.<sup>27–29</sup> Small crystal sediments in the glass container were visible to the eyes (Fig. 2a). When the CPAMAM was used as a stabilizer in alkaline condition, the Ca/P mixture formed ACP nanoparticles of about 30 nm in size, which aggregate to form agglomerates, as shown in Fig. 2b1 and b2. These agglomerates further transformed to crystal phase after incubation for 30 min (Fig. 2b3 and b4). When the CPAMAM was used in weak acidic condition, the ACP formed dispersed nanoparticles of 4 nm in size and no sediments were visible in the glass container, as shown in Fig. 2c1 and c2. These ACP nanoparticles grew to about 25 nm after incubating the Ca/P/



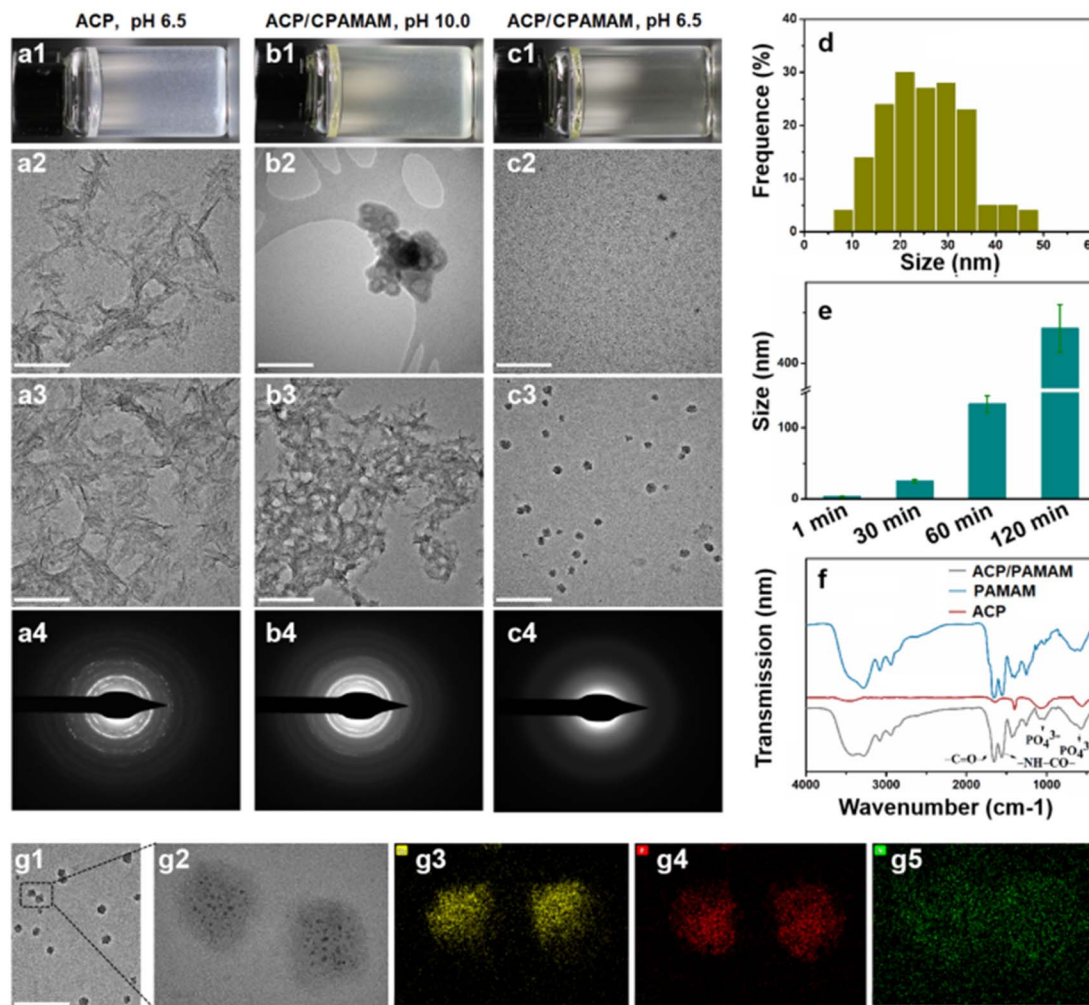


Fig. 2 Preparation of ACP nanoparticles with three different formulas. (a1–c1) Reaction mixtures for preparing ACP under weakly acidic condition (a1), ACP/CPAMAM under alkaline condition (b1), and ACP/CPAMAM under weak acidic condition (c1). (a2–c2) Representative TEM images of the above three ACP formulas with reaction time of 1 min. Scale bar: 200 nm. (a3–c3) Representative TEM images of the above three ACP formulas with reaction time of 30 min. (a4–c4) Selected area electron diffraction of the three ACP formulas from a3–c3. (d) Size distribution of ACP/CPAMAM prepared under weak acidic condition for various reaction times. (e) The average size of the ACP/CPAMAM prepared under weak acidic condition for various reaction times. (f) Infrared spectra of the ACP/CPAMAM. (g1–g5) STEM-EDX mapping for calcium (g3), phosphorus (g4), and nitrogen (g5) of the ACP/CPAMAM nanoparticles.

CPAMAM mixture for 30 min (Fig. 2c3 and c4). The size distribution of the ACP nanoparticles ranged from 10 to 40 nm (Fig. 2d), which is smaller than the gap of the collagen.

Fig. 2e and ESI Fig. S1† show the average size of the ACP nanoparticles prepared in various reaction times. The size of the ACP nanoparticles could be controlled by changing the reaction time of the Ca/P/CPAMAM mixture. When the reaction time increased to 60 min, the formed ACP nanoparticles were too large to enter the gap of the collagen. Hence, we chose 30 min as the optimal reaction time for the subsequent experiments. The FTIR spectra of ACP/CPAMAM are shown in Fig. 2f. The absorption peaks at 1246, 1517 and 1650  $\text{cm}^{-1}$  corresponded to the stretching vibrations of amide bond of the CPAMAM, and the peak at 1075  $\text{cm}^{-1}$  was assigned to  $\text{PO}_4^{3-}$ . All these characteristic peaks were present in the spectrum for ACP/CPAMAM group. STEM-EDX mapping showed colocalization of

calcium (from ACP), phosphorus (from ACP), and nitrogen (from CPAMAM), as shown in Fig. 2g1–g5. Both FTIR and STEM-EDX demonstrated the incorporation of ACP and CPAMAM to form ACP/CPAMAM nanoparticles. These results indicated the ACP nanoparticles with good monodispersity were successfully prepared by using CPAMAM as a stabilizer in weak acidic condition.

### 3.2. The ACP/CPAMAM nanoparticles were loaded into micelles

Although the ACP could be stabilized transiently by CPAMAM to form dispersed ACP/CPAMAM nanoparticles, they were likely to aggregate after storage for a period of time due to the low zeta potential of the nanoparticles ( $-6$ ). In order to improve the storage stability of the ACP/CPAMAM nanoparticles and expand their practical applications, we used polysorbate combined with



PEG to separate the ACP/CPAMAM nanoparticle from each other. As a surfactant, polysorbate would self-assemble to form micelles in aqueous phase,<sup>30</sup> during which the ACP/CPAMAM nanoparticles were supposed to be included in the micelles. Meanwhile, PEG was used to stabilize the micelles in aqueous phase.

As shown in Fig. 3a, micelles with size ranging from 100 to 250 nm were assembled when polysorbate solution of 100 mg mL<sup>-1</sup> was ultrasonic agitated with the ACP/CPAMAM for 3 h. The ACP/CPAMAM nanoparticles were successfully loaded into the micelles. The size of the micelles and the loading efficiency of the ACP/CPAMAM in the micelles increased with the increasing of polysorbate concentration, as shown in Fig. 3b–3d. However, when the polysorbate concentration reached to 500 mg mL<sup>-1</sup>, lots of unloaded micelles appeared. Hence, we took 350 mg mL<sup>-1</sup> as the optimal polysorbate concentration, where a loading rate of 40% and an average size of 303 nm were obtained (Fig. 3e). The Raman peaks for PO<sub>4</sub><sup>3+</sup> at 532 cm<sup>-1</sup>, 600 cm<sup>-1</sup>, and 960 cm<sup>-1</sup> indicated the presence of ACP in the micelles, as shown in Fig. 3f. A representative micelle containing four ACP/CPAMAM nanoparticles was analyzed by STEM-EDX mapping, as shown in Fig. 3g1–g4. The phosphorus and

calcium spots in the micelle were colocalized with the ACP/CPAMAM nanoparticles, further indicating the ACP were loaded into the micelles.

### 3.3. The micelles-loaded ACP/CPAMAM nanoparticles showed good storage stability

The micelles-loaded ACP/CPAMAM nanoparticle solutions were stored at 4 °C in refrigerator for different times. Fig. 4 shows the comparison of storage stability for various ACP formulas. Without CPAMAM, the ACP aggregated and transformed to crystal phase rapidly even in the present of micelle (Fig. 4a1 and a2). The CPAMAM could stabilize the ACP nanoparticles and hence prevented them from crystal phase transition (Fig. 4b1). However, after storage for 30 days, the CPAMAM stabilized ACP (ACP/CPAMAM) nanoparticles aggregated to form sediments (Fig. 4b2), which was no longer acceptable for intrafibrillar mineralization. When the ACP/CPAMAM nanoparticles were loaded into the micelles, the ACP maintained amorphous phase even after storage for 12 months, as shown in Fig. 4c1–c4. These results demonstrated that the micelles could block the collision between the ACP/CPAMAM nanoparticles by separating the

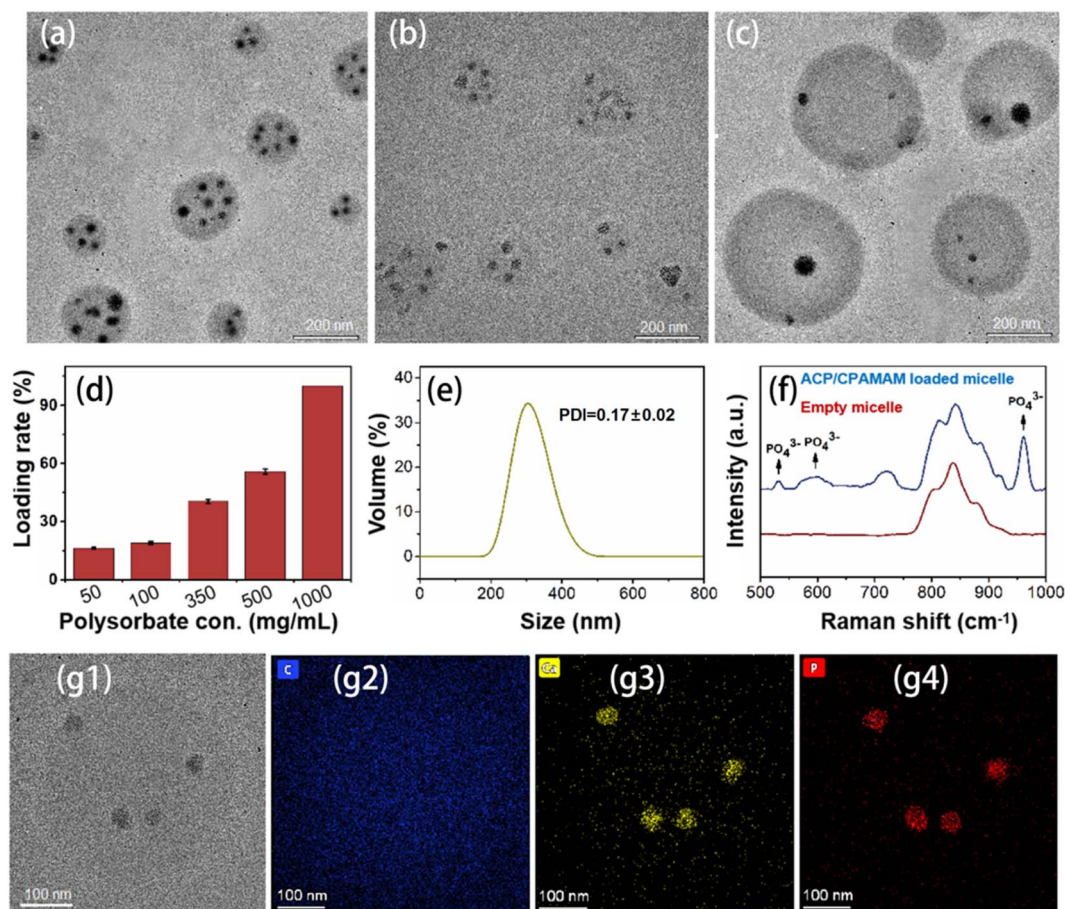


Fig. 3 Assembling of micelle-loaded ACP/CPAMAM. (a–c) TEM images of the micelle-loaded ACP/CPAMAM nanoparticles, with polysorbate concentrations of 100 mg mL<sup>-1</sup> (a), 350 mg mL<sup>-1</sup> (b), and 500 mg mL<sup>-1</sup> (c). (d) Loading rate of the ACP/CPAMAM in the micelles under various polysorbate concentrations. (e and f) The size distribution (e) and Raman spectrum (f) of the micelles, with polysorbate concentrations of 350 mg mL<sup>-1</sup> (g1–g4) STEM-EDX mapping for carbon, calcium and phosphorus of the micelle.



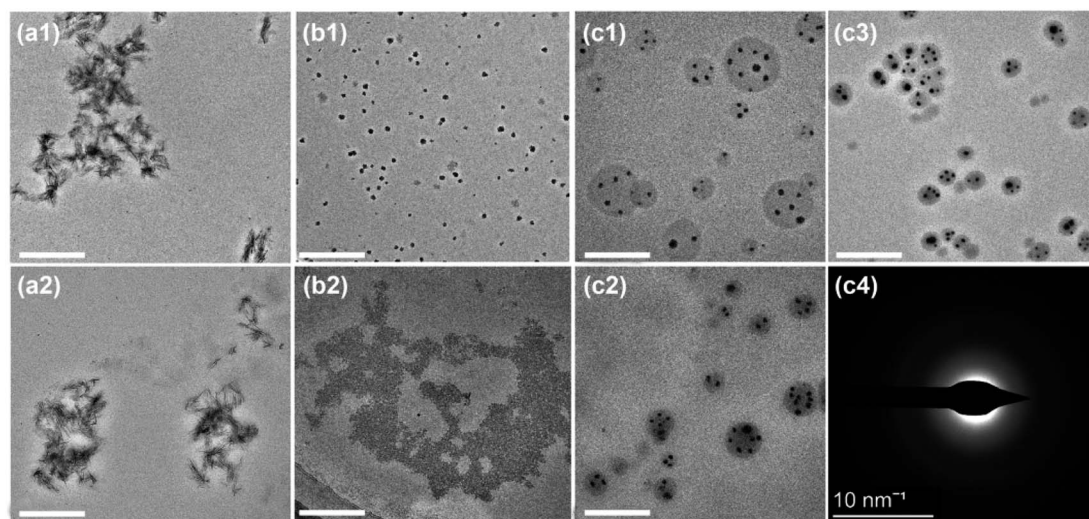


Fig. 4 Comparison of storage stability between the ACP/CPAMAM and micelle-loaded ACP/CPAMAM. (a1–c1) Representative TEM images of micelle-loaded ACP (a1), ACP/CPAMAM (b1), and micelle-loaded ACP/CPAMAM (c1) stored for one day. (a2–c2) The above three ACP formulas after storing for 30 days. (c3) Micelle-loaded ACP/CPAMAM after storing for one year. (c4) Selected area electron diffraction of the micelle-loaded ACP/CPAMAM after storing for one year. Scale bar: 200 nm.

particles from each other. Meanwhile, the CPAMAM kept the ACP at amorphous phase. The combined use of CPAMAM and micelle enable us to keep the ACP monodispersed at amorphous phase.

### 3.4. Controlled release of ACP/CPAMAM nanoparticles from the micelles

When the micelle-loaded ACP/CPAMAM is used for mineralization, the ACP/CPAMAM nanoparticles need to be released

from the micelles. Isopropanol (IPA), as a lipolytic reagent, could sharply decrease the surface tension of lipoid polysorbate in aqueous phase,<sup>31</sup> which might lead to the dissolution of the micelles. Hence, we use IPA of various concentrations to destroy the micelles and release the ACP/CPAMAM nanoparticles, as shown in Fig. 5a–5d. When 0.1 g mL<sup>-1</sup> IPA was added to the micelle-loaded ACP/CPAMAM, some micelles were just under cracking (Fig. 5b). When the IPA increased to 0.2 g mL<sup>-1</sup>, nearly all the ACP nanoparticles released to the solutions (Fig. 5c). The

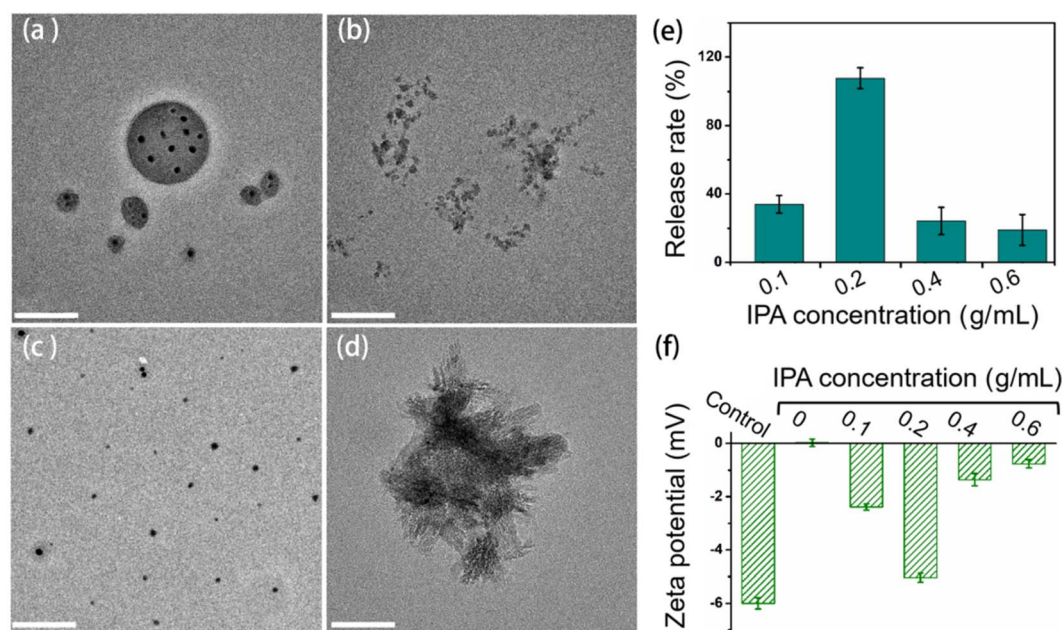
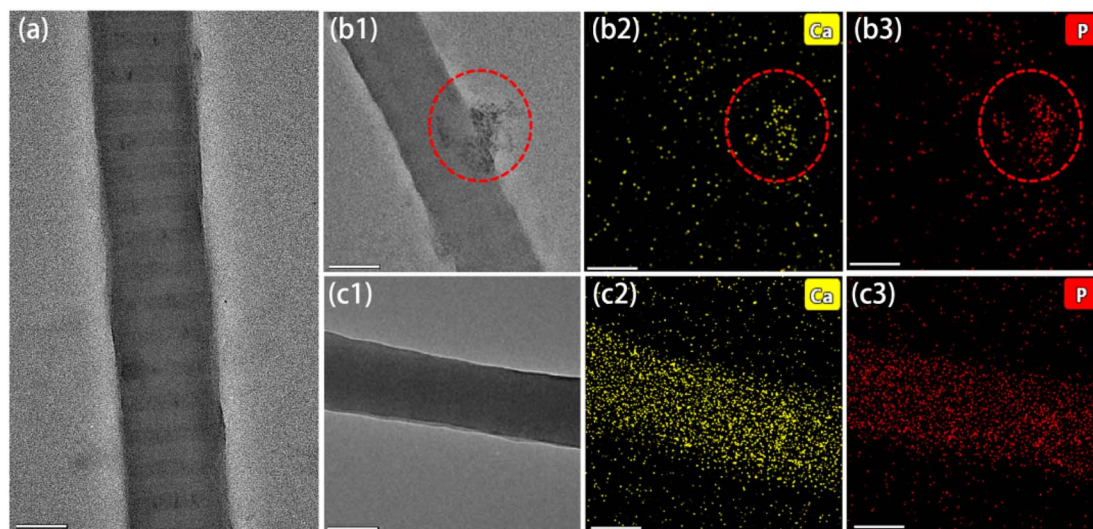


Fig. 5 Release of ACP/CPAMAM nanoparticles from the micelles. (a) Micelle-loaded ACP/CPAMAM. (b–d) Micelle-loaded ACP/CPAMAM with the addition of 0.1 g mL<sup>-1</sup> (b), 0.2 g mL<sup>-1</sup> (c), and 0.4 g mL<sup>-1</sup> (d) IPA. Scale bar: 200 nm. (e) Release rate of the ACP/CPAMAM in the micelles under various IPA concentrations. (f) Zeta potentials of the micelle-loaded ACP/CPAMAM solution under various IPA concentrations. Freshly prepared ACP/CPAMAM without micelles was measured as a control.





**Fig. 6** Intrafibrillar mineralization of type I collagen by micelle-loaded ACP/CPAMAM nanoparticles. (a) TEM image of reconstituted collagen fibril without mineralization. (b1–c1) TEM images of reconstituted collagen fibrils mineralized directly by Ca/P mixture (b1, as control), and micelle-loaded ACP/CPAMAM (c1) for 5 days. (b2–c2) and (b3–c3) STEM-EDX mapping for calcium and phosphorus of the above samples. Scale bar: 200 nm.

released ACP/CPAMAM particles could be separated from the micelles thorough centrifugation at 10 000 ref for 60 min, the supernatant of which was subjected to calcium content analysis for release rate determination. Theoretically, there should be a positive correlation between the released ACP/CPAMAM nanoparticles and the IPA concentration used for cracking the micelles. However, it was worth noting that the IPA could accelerate the transformation of ACP from amorphous phase to crystal phase. High IPA concentration led to the rapid agglomeration of the ACP and formation of crystal phase, as shown in Fig. 5d. The agglomeration and crystallization resulted in the low release rate of the ACP (Fig. 5d and e). In addition, the ACP/

CPAMAM nanoparticles released by 0.2 g mL<sup>-1</sup> IPA had a similar zeta potential with that of freshly prepared ACP/CPAMAM nanoparticles, as shown in Fig. 5f, indicating they had similar colloidal stability. These results indicated the release of ACP/CPAMAM nanoparticles from the micelles could be controlled by adding IPA, with an optimal concentration of 0.2 g mL<sup>-1</sup>.

### 3.5. Mineralization of collagen by micelle-loaded ACP/CPAMAM nanoparticles

To demonstrate the mineralization function of the micelle-loaded ACP/CPAMAM, self-assembled type I collagen fibrils

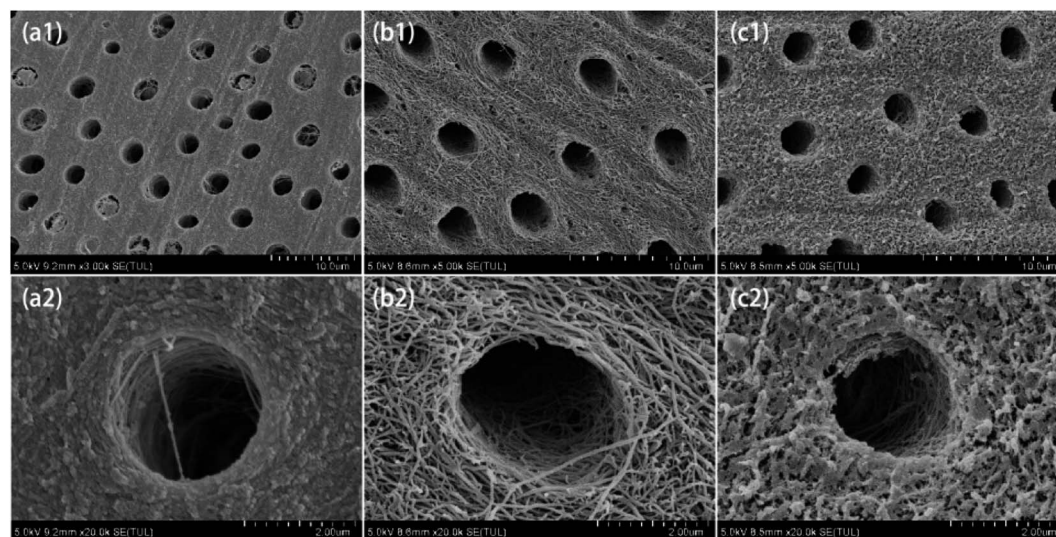


**Fig. 7** Extrafibrillar mineralization of dentin by micelle-loaded ACP/CPAMAM. (a1, a2) Natural dentin. (b1, b2) Demineralized dentin. (c1, c2) Remineralized dentin, which was mineralized by micelle-loaded ACP/CPAMAM for 15 days. (a2), (b2) and (c2) are the enlarged images of (a1), (b1) and (c1), respectively.



were exposed to the micelle-loaded ACP/CPAMAM for 5 days, during which IPA was introduced to release the ACP/CPAMAM nanoparticles from the micelles at pH of 6.5. Then ACP particles smaller than 40 nm initially infiltrate into the gaps of the collagen, as described in Fig. 1. By adjusting the pH of the system from 6.5 to 10.0, the ACP particles transformed into thermodynamically stable HAP.

The reconstituted collagen fibrils without mineralization showed stripe-like gaps, with a size of about 50 nm, as shown in Fig. 6a. When Ca/P mixture (ACP) was directly used for mineralization, the ACP transformed fleetly to crystal phase before entering into the gaps of the collagen, leading to failure in intrafibrillar mineralization. As a result, few calcium and phosphorus dots deposited along with the collagen fibrils, as shown in Fig. 6b1–b3. The red circles in Fig. 6b1–b3 showed the extrafibrillar deposition of HAP crystal, which could not enter the gap of the collagen. When the micelle-loaded ACP/CPAMAM was used, the intrafibrillar mineralization of collagen was accomplished by infiltrating the ACP/CPAMAM nanoparticles into the collagen fibrils *via* gap zones. After intrafibrillar mineralization, Ca and P distributed uniformly through the whole fibril, as shown in Fig. 6c1–c3. As a result, the electron density of the TEM image was uniform and the stripe-like gaps were disappeared (Fig. 6c1).

For teeth repairing and bone reconstruction, both intrafibrillar and extrafibrillar mineralizations are expected to obtain artificial biominerals with structure and function as similar to natural ones as possible. Hence, demineralized teeth were used to further evaluate the extrafibrillar mineralization effect of the micelle-loaded ACP/CPAMAM. As shown in Fig. 7a1 and a2, natural dentin showed a dense structure, with type I collagen filled with HAP both internally and externally. Once being demineralized by EDTA, the net-like collagen fibrils were exposed as shown in Fig. 7b1 and b2. After remineralization for 15 days by the micelle-loaded ACP/CPAMAM, the collagen fibril nets were refilled with HAP as shown in Fig. 7c1, c2 and ESI Fig. S2,<sup>†</sup> indicating the successful extrafibrillar mineralization of the collagen. However, there were still many micropores remaining in the fibril nets, and mineralization time need to be prolonged to cover all the interspaces of the fibrils.

## 4. Conclusions

Mineralization of collagen fibrils is of great importance for assembling biomimetic bones. As the most widely used mineralization reagent, amorphous calcium phosphates (ACPs) were extremely unstable. They are likely to aggregate and transform to crystalline phase before entering into the gaps of intrafibrillar and extrafibrillar collagen. In this study, we firstly assembled ACP nanoparticles, which were stabilized by carboxylated polyamidoamine (CPAMAM) at slight acidic environment to form monodispersed ACP/CPAMAM nanoparticles. The ACP/CPAMAM nanoparticles were further loaded into micelles composed of polysorbate and PEG, which prevent the ACP nanoparticles from aggregation and prolong their storage time. When the micelle-loaded ACP/CPAMAM was used for mineralization of collagen, IPA was added to destroy the

micelles and release the ACP/CPAMAM nanoparticles, which then entered the gaps of the collagen for both intrafibrillar and extrafibrillar mineralization. Good mineralization results were demonstrated by *in vivo* extrafibrillar mineralization and *in vitro* intrafibrillar mineralization experiments.

## Author contributions

Hongyu Xie and Jian Sun: investigation & writing. Fangfang Xie: investigation & funding acquisition. Shengbin He: conceptualization, writing-review & editing, project administration.

## Conflicts of interest

No potential conflict of interest is reported by the authors.

## Acknowledgements

The authors are grateful for the financial support provided by the National Natural Science Foundation of China (Grants 82260190) and Innovation Project of Guangxi Graduate Education (Grants YCSW2022216).

## References

- W. Yan, T. Azas, M. Robin, A. Vallée, C. Catania, P. Legriel, G. Pehau-Arnaudet, F. Babonneau, M. M. Giraud-Guille and N. Nassif, The predominant role of collagen in the nucleation, growth, structure and orientation of bone apatite, *Nat. Mater.*, 2012, **11**, 724–733.
- Q. Song, K. Jiao, L. Tonggu, L. G. Wang, S. L. Zhang, Y. D. Yang, L. Zhang, J. H. Bian, D. X. Hao and C. Y. Wang, Contribution of biomimetic collagen-ligand interaction to intrafibrillar mineralization, *Sci. Adv.*, 2019, **5**(3), eaav9075.
- B. M. Oosterlaken, M. P. Vena and G. D. With, In vitro mineralization of collagen, *Adv. Mater.*, 2021, **33**(16), e2004418.
- W. E. Roberts, J. E. Mangum and P. M. Schneider, Pathophysiology of demineralization, part I: attrition, erosion, abfraction, and noncarious cervical lesions, *Curr. Osteoporosis Rep.*, 2022, **20**(1), 90–105.
- Z. Akram, S. Aati, H. Ngo and A. Fawzy, pH-dependent delivery of chlorhexidine from PGA grafted mesoporous silica nanoparticles at resin-dentin interface, *J. Nanobiotechnol.*, 2021, **19**(1), 43.
- X. Cai, B. Han, Y. Liu, F. Tian, F. Liang and X. Wang, Chlorhexidine-Loaded Amorphous Calcium Phosphate Nanoparticles for Inhibiting Degradation and Inducing Mineralization of Type I Collagen, *ACS Appl. Mater. Interfaces*, 2017, **9**(15), 12949–12958.
- L. Chen, W. Chen, Y. Yu, J. Yang and D. Yang, Effect of chlorhexidine-loaded poly(amido amine) dendrimer on matrix metalloproteinase activities and remineralization in etched human dentin *in vitro*, *J. Mech. Behav. Biomed. Mater.*, 2021, **121**(6), 104625.



- 8 S. Tang, Z. Dong, X. Ke, J. Luo and J. Li, Advances in biomineralization-inspired materials for hard tissue repair, *Int. J. Oral Sci.*, 2021, **13**(1), 42.
- 9 S. Langhorst, J. O'Donnell and D. Skrtic, In vitro remineralization of enamel by polymeric amorphous calcium phosphate composite: quantitative microradiographic study, *Dent. Mater.*, 2009, **25**, 884–891.
- 10 K. Liang, M. D. Weir, X. Xie, L. Wang, M. A. Reynolds, J. Li and H. H. K. Xu, Dentin remineralization in acid challenge environment via PAMAM and calcium phosphate composite, *Dent. Mater.*, 2016, **32**(11), 1429–1440.
- 11 M. D. Weir, L. C. Chow and H. H. Xu, Remineralization of demineralized enamel via calcium phosphate nanocomposite, *J. Dent. Res.*, 2012, **91**, 979–984.
- 12 S. Xiao, K. Liang, M. D. Weir, L. Cheng, H. Liu, X. Zhou, Y. Ding and H. H. K. Xu, Combining bioactive multifunctional dental composite with PAMAM for root dentin remineralization, *Materials*, 2017, **10**, 89.
- 13 Y. K. Kim, L. S. Gu, T. E. Bryan, J. R. Kim, L. Chen, Y. Liu, J. C. Yoon, L. Breschi, D. H. Pashley and F. R. Tay, Mineralisation of reconstituted collagen using polyvinylphosphonic acid/polyacrylic acid templating matrix protein analogues in the presence of calcium, phosphate and hydroxyl ions, *Biomaterials*, 2010, **31**(25), 6618–6627.
- 14 M. Wang, H. Deng, T. Jiang and Y. Wang, Biomimetic remineralization of human dentine via a “bottom-up” approach inspired by nacre formation, *Biomater. Adv.*, 2022, **135**, 112670.
- 15 Z. Chen, Y. Duan, S. Shan, K. Sun, G. Wang, C. Shao, Z. Tang, Z. Xu, Y. Zhou, Z. Chen, R. Tang, H. Pan and Z. Xie, Deep and compact dentinal tubule occlusion via biomimetic mineralization and mineral overgrowth, *Nanoscale*, 2022, **14**(3), 642–652.
- 16 C. Robinson, Self-oriented Assembly of Nano-apatite Particles: a Subunit Mechanism for Building Biological Mineral Crystals, *J. Dent. Res.*, 2007, **86**(8), 677–679.
- 17 M. Keskar, C. Sabatini, C. Cheng and M. T. Swihart, Synthesis and characterization of silver nanoparticle-loaded amorphous calcium phosphate microspheres for dental applications, *Nanoscale Adv.*, 2019, **1**, 627–635.
- 18 L. Niu, S. E. Jee, K. Jiao, L. Tonggu, M. Li, L. Wang, Y. Yang, J. Bian, L. Breschi, S. S. Jang, J. Chen, D. H. Pashley and F. R. Tay, Collagen intrafibrillar mineralization as a result of the balance between osmotic equilibrium and electroneutrality, *Nat. Mater.*, 2017, **16**, 370–378.
- 19 L. Niu, W. Zhang, D. H. Pashley, L. Breschi, J. Mao, J. Chen and F. R. Tay, Biomimetic remineralization of dentin, *Dent. Mater.*, 2014, **30**, 77–96.
- 20 K. Jiao, L. N. Niu, C. F. Ma, X. Q. Huang, D. D. Pei, T. Luo, Q. Huang, J. H. Chen and F. R. Tay, Collagen mineralization: complementarity and uncertainty in intrafibrillar mineralization of collagen, *Adv. Funct. Mater.*, 2016, **26**(38), 6850.
- 21 Y. X. Ma, S. E. Hoff, X. Q. Huang, J. Liu and L. N. Niu, Involvement of prenucleation clusters in calcium phosphate mineralization of collagen, *Acta Biomater.*, 2020, **120**, 213–223.
- 22 A. George, B. Sabsay, P. A. L. Simonian and A. Veis, Characterization of a novel dentin matrix acidic phosphoprotein. Implications for induction of biomineralization, *J. Biol. Chem.*, 1993, **268**(7), 12624–12630.
- 23 M. Hernandez, D. Cobb and E. J. Swift, Guided tissue remineralisation of partially demineralised human dentin, *J. Esthet. Restor. Dent.*, 2014, **26**(2), 141–142.
- 24 S. S. Jee, T. T. Thula and L. B. Gower, Development of bone-like composites via the polymer induced liquid-precursor (PILP) process. Part 1: influence of polymer molecular weight, *Acta Biomater.*, 2010, **6**(9), 3676–3686.
- 25 F. Xie, J. Long, J. Yang, H. Qin, X. Lin and W. Chen, Effect of a new modified polyamidoamine dendrimer biomimetic system on the mineralization of type I collagen fibrils: an in vitro study, *J. Biomater. Sci., Polym. Ed.*, 2022, **33**(2), 212–228.
- 26 X. Cai and X. Wang, Chlorhexidine-loaded poly (amido amine) dendrimer and a dental adhesive containing amorphous calcium phosphate nanofillers for enhancing bonding durability, *Dent. Mater.*, 2022, **38**(5), 824–834.
- 27 C. Shao, R. A. Bapat, J. Su and J. Moradian Oldak, Regulation of hydroxyapatite nucleation in vitro through ameloblastin–amelogenin interactions, *ACS Biomater. Sci. Eng.*, 2023, **9**(4), 1834–1842.
- 28 E. Ruiz-Agudo, C. Ruiz-Agudo, F. Di Lorenzo, P. Alvarez-Lloret, A. Ibañez-Velasco and C. Rodriguez-Navarro, Citrate stabilizes hydroxylapatite precursors: implications for bone mineralization, *ACS Biomater. Sci. Eng.*, 2021, **7**(6), 2346–2357.
- 29 R. Chang, Y. J. Liu, Y. L. Zhang, S. Y. Zhang, B. B. Han, F. Chen and e. al, Phosphorylated and Phosphonated Low-Complexity Protein Segments for Biomimetic Mineralization and Repair of Tooth Enamel, *Adv. Sci.*, 2022, **9**(6), e2103829.
- 30 H. Aizawa, Morphology of polysorbate 80 (Tween 80) micelles in aqueous 1,4-dioxane solutions, *J. Appl. Crystallogr.*, 2009, **42**(4), 592–596.
- 31 L. Hao, B. Jiang, L. Zhang, H. Yang, Y. Sun, B. Wang and N. Yang, Efficient demulsification of diesel-in-water emulsions by different structural dendrimer-based demulsifiers, *Ind. Eng. Chem. Res.*, 2016, **55**(6), 1748–1759.

